CHAPTER 5

Modeling studies of the methane steam reforming reaction at high pressure in a ceramic membrane reactor

5.1. Introduction

In this chapter, additional experimental studies of the steam reforming of methane were examined at various temperatures (773-923 K) and pressures (1-20 atm) in a hydrogen selective alumina-silica membrane reactor and a packed-bed reactor. One-dimensional and two-dimensional modeling of the membrane rector and the packed-bed reactor were performed at the same conditions and their performances were compared with the values obtained experimentally. Improved methane conversions and hydrogen yields were obtained in the membrane reactor than the packed-bed reactor at all temperatures and pressures. From the two modeling studies, it was also found out that the two-dimensional model performed better in the membrane reactor case when compared to the one-dimensional model, especially at higher pressures. The estimation of radial flow terms by the two-dimensional model accounted for mass transfer through the membrane and resulted in much closer agreement with the experimental quantities.

5.2. Experimental

5.2.1. Preparation of $Ni/MgAl_2O_4$ catalysts

The $Ni/MgAl_2O_4$ catalysts (NG-610-6H) similar to those reported in Chapter 4 were used in these studies. A lower quantity of 0.05 g of this catalyst was mixed with 2.0 g of inert quartz chips of the same size to make a catalyst bed of 5 cm length this time.

5.2.2. Hydrogen selective silica based membranes

Hydrogen selective alumina-silica membranes similar to those described in detail in Chapter-1 were used in these studies. The hydrogen selective layer was obtained by further deposition of tetraethylorthosilicate (TEOS, Aldrich, 98%) and aluminum-tri-sec-butoxide (ATSB, Aldrich, 97%) in argon flow at 923 K simultaneously. The alumina support was first placed concentrically in a tubular quartz reactor (ID = 14 mm) by using Swagelok fittings equipped with Teflon ferrules and then installed in a split tube furnace and heated to 923 K with a ramp of 1 K/ min (Figure 2.1). When the desired temperature of 923 K was reached, argon flow was introduced on both the shell side and the tube side of the reactor. The TEOS concentration was set to 0.0194 mol/ m^3 by flowing argon gas through a bubbler which was kept at 298 K and the ATSB concentration was set to 0.000582 mol/ m^3 in a similar manner except that the bubbler was kept at 363 K in an oil bath. These carrier flows were introduced to the tube side of the reactor. All the carrier and dilute gas flows were adjusted by mass flow controllers (Brooks Model 5850E). The

permeance of gases (H_2, CH_4, CO, CO_2) and the selectivity of hydrogen over other gases were measured at predetermined intervals. The deposition process was continued until the hydrogen permeance through the membrane reached a value of 2.0×10^{-7} mol m^{-2} s^{-1} Pa^{-1} at 923 K. Hydrothermal stability tests showed that the gas separation performance of the silica-alumina membrane was stable under harsh conditions of the steam reforming reaction.

5.2.3. Steam reforming of methane in a membrane reactor

The steam reforming of methane in both the PBR and the MR similar to those reported in Chapter-4 was carried out at various temperatures (873, 923 K) and pressures (1-20 atm). The flow rates of methane and steam were doubled in this study with the overall flow rate of the reactants increasing in proportion to the pressure to keep the residence time constant (Table 5.1).

Table 5.1. Inlet flow rates of the reactants

Pressure (atm)	Volumetric flow rate of CH_4 (cm^3 (NTP) min^{-1})	Volumetric flow rate of H_2O (cm^3 (NTP) min^{-1})
1	10	30
5	50	150
10	100	300
15	150	450
20	200	600

5.2.4. Modeling of steam reforming of methane in a membrane reactor

In this study the steam reforming of methane (SRM) was described by the two reversible reactions (Reaction 1 and 3) and the water gas shift (WGS) reaction (Reaction 2) presented earlier.

A Ni/ $MgAl_2O_4$ catalyst was chosen for this study because the kinetics of the methane steam reforming and water-gas shift reactions on a catalyst of the same composition were already reported by Xu and Froment [1]. The kinetic rate expressions for the three reactions were based on a Langmuir-Hinshelwood reaction mechanism which contained 13 steps and was proved to be the most general for these nickel catalysts. The rate expressions and equilibrium constants for the reactions (1-3) are presented in Table 5.2. The expressions for the reaction rate and adsorption constants are given in Table 5.3. The term containing the partial pressure of hydrogen in the denominator of the above equations originated from the equilibrium between hydrogen in the gas phase and dissociatively adsorbed hydrogen. In order to apply these equations, hydrogen should be present in the feed stream to make the initial rate of methane conversion finite. Thus, the arbitrary value of 10^{-10} for P_{H2} /P_{CH4} was chosen in the present kinetic model.

Table 5.2. Reaction rates and equilibrium constants for MSR and WGS reactions

Reaction rates:

$$r_1 = \frac{\frac{k_1}{P_{H_2}^{2.5}}\left[P_{CO}P_{H_2O} - \frac{P_{H_2}^3 P_{CO}}{K_{eq1}}\right]}{DEN^2}$$

$$r_2 = \frac{\frac{k_2}{P_{H_2}}\left[P_{CO}P_{H_2O} - \frac{P_{H_2}P_{CO_2}}{K_{eq2}}\right]}{DEN^2}$$

$$r_3 = \frac{\frac{k_3}{P_{H_2}^{3.5}}\left[P_{CH_4}P_{H_2O}^2 - \frac{P_{H_2}^4 P_{CO_2}}{K_{eq3}}\right]}{DEN^2}$$

$$DEN = 1 + K_{CO}P_{CO} + K_{H_2}P_{H_2} + K_{CH_4}P_{CH_4} + K_{H_2O}\frac{P_{H_2O}}{P_{H_2}}$$

Equilibrium constants:

Temperature (K)	K_1	K_2
873	0.4985	2.527
923	2.649	1.931

Table 5.3. Adsorption constants

Reaction rate constants:

$$k_i = A_i exp\left(\frac{-E_i}{RT}\right) \qquad i = 1, 2, 3$$

Reaction	A_i (mol bar$^{0.5}$/ gcat s)	E_i (J/mol)
1	1.174×10^{12}	240100
2	5.43×10^{2}	67130
3	2.833×10^{11}	243900

Adsorption constants:

$$K_j = B_j exp\left(\frac{-\Delta H_j}{RT}\right) \qquad j = CO, H_2, CH_4, H_2O$$

Species	Bj (bar^{-1})	ΔHj (J/mol)
CO	8.23×10^{-5}	-70650
H_2	6.12×10^{-9}	-82900
CH_4	6.65×10^{-4}	-38280
H_2O	1.77×10^{5}	88680

A schematic of the reaction model used for the simulation of the membrane reactor is shown in Figure 5.1. The one-dimensional modeling of the membrane reactor was based on the following assumptions: 1) Steady-state conditions and plug flow in both the reaction and permeation sides, 2) Negligible pressure drop along the axial direction,

3) Isothermal conditions. The molar flow rates of the species in the shell and tube sides in a membrane reactor are described in Table 5.4. They were calculated by solving the set of the ODE's, with the IMSL subroutine DIVPAG found in the DMATHD and DMATHS library of MSDEV (Microsoft Developer Studio).

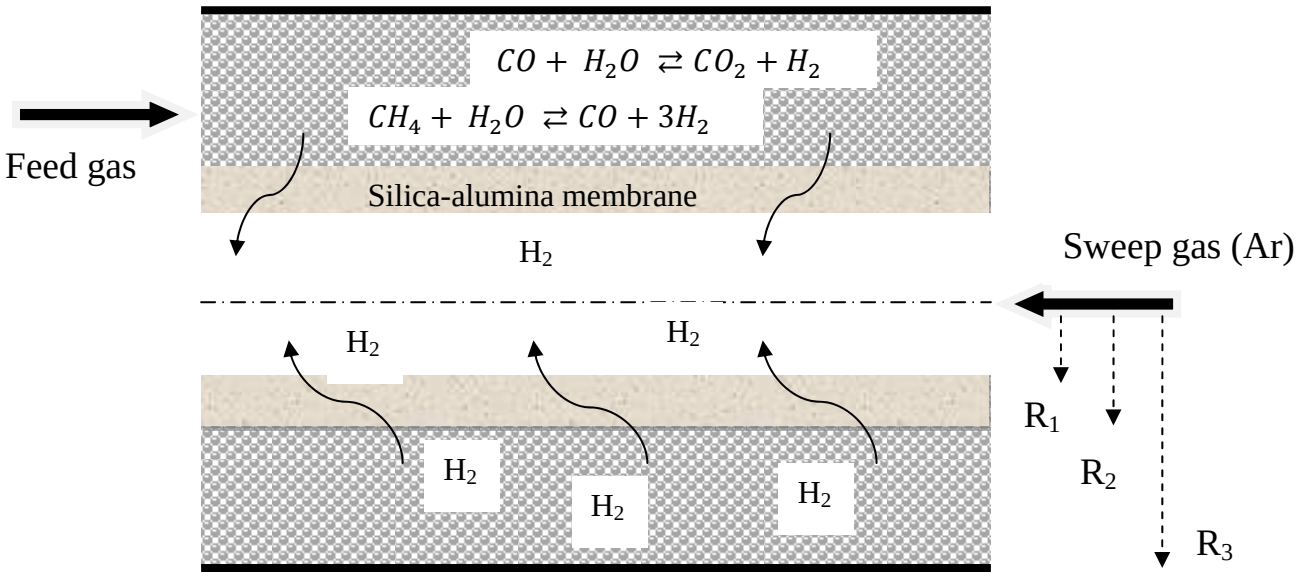

Figure 5.1. Schematic reaction system model for simulations

The two-dimensional modeling of the membrane reactor was based on model equations and boundary conditions derived from a mass balance for each component in each region as described in Table 5.5. The two-dimensional model was developed with the following assumptions: 1) Isobaric reactor conditions, 2) cylindrical symmetry, 3) diffusive and convective radial transport and 4) convective axial transport. Table 5.6 presents the relevant dimensionless quantities used in the model, and the dimensionless forms of partial differential equations.

Table 5.4. Model equations for the one-dimensional model

Tube side:	Shell side:
$\frac{dF_i}{dw} = R_i^{perm}$	$\frac{dF_i}{dw} = \sum_{j=1,2,3} \gamma_{i,j} R_j - R_i^{perm}$
$where \qquad R_i^{perm} = S_i a\left(P_i^{shell} - P_i^{tube}\right)$	
Initial conditions:	
Tube side:	Shell side:
$F_{Ar} = F_{Ar}^o$	$F_{CH_4} = F_{CH_4}^o, F_{H_2O} = F_{H_2\,O}^o, F_{H_2} = F_{H_2}^o$

Binary diffusivities were estimated by using two equations, the first of which estimated the binary diffusivity coefficients where water vapor was one of the components and the second estimated the rest of the pairs (Table 5.7). The equation utilized the critical temperatures and pressures of the gases. Effective diffusivities were then estimated from the binary diffusivity coefficients as shown in Table 7. Linear velocities were predicted in every step from the concentrations of the species in the reaction. Partial pressures were calculated in every step of the simulation and used in determining the rates of the reaction.

The dimensionless concentrations were obtained by solving the set of the ODE's, with the IMSL subroutine DIVPAG found in the DMATHD and DMATHS library of MSDEV (Microsoft Developer Studio). The partial differential equations were redefined as a set of ODE's by using finite difference approximations and these ODE's were

divided into nodes in the radial direction so that the subroutine can solve the equations both in the axial and radial coordinates.

Table 5.5. Model equations for the two-dimensional model

Tube side:	Shell side:
$D_{1i}\left(\frac{\partial^2 C_{1i}}{\partial r^2}+\frac{1}{r}\frac{\partial C_{1i}}{\partial r}\right)-u_1\frac{\partial C_{1i}}{\partial l}=0$	$\varepsilon_{3i}D_{3i}\left(\frac{\partial^2 C_{3i}}{\partial r^2}+\frac{1}{r}\frac{\partial C_{3i}}{\partial r}\right)-u_3\frac{\partial C_{3i}}{\partial l}-\Sigma Rkn=0$
Boundary conditions:	
$at\ r=0\ (center\ of\ the\ tube\ side)$	$at\ r=R_2\ (membrane\ surface\ in\ the\ shell\ side)$
$\frac{\partial C_{1i}}{\partial r}=0$	$S_{3i}\,P\,(C_{is}-C_{it})=\frac{\partial C_{3i}}{\partial r}$
$at\ r=R_1\ (membrane\ surf.in\ the\ tube\ side)$	$at\ r=R_3(reactor\ wall\ in\ the\ shell\ side)$
$\frac{\partial C_{1i}}{\partial r}=S_{1i}\,P\,(C_{is}-C_{it})$	$\frac{\partial C_{3i}}{\partial r}=0$
Initial conditions:	
Tube side:	Shell side:
$C_{Ar}=C_{Ar,0}$	$C_{CH_4}=C_{CH_4,0},\quad C_{H_2O}=C_{H_2O,0},\quad C_{H_2}=C_{H_2,0}$

Table 5.6. Dimensionless quantities and dimensionless model equations

Dimensionless quantities:

$0 \le r \le R_1 \qquad \bar{r} = \dfrac{r}{R_1}$

$R_1 \le r \le R_2 \qquad \bar{r} = \dfrac{r - R_1}{R_2 - R_1}$

$R_2 \le r \le R_3 \qquad \bar{r} = \dfrac{r - R_2}{R_3 - R_2}$

$\overline{C_{j\imath}} = \dfrac{C_{ji}}{C^0_{CH_4}}$

$\bar{l} = \dfrac{l}{L}$

Tube side:

$$\overline{D_{1\imath}}\left(\frac{\partial^2 \overline{C_{1\imath}}}{\partial \bar{r}^2} + \frac{1}{\bar{r}}\frac{\partial \overline{C_{1\imath}}}{\partial \bar{r}}\right) - \frac{\partial \overline{C_{1\imath}}}{\partial \bar{l}} = 0$$

$where \qquad \overline{D_{1\imath}} = \dfrac{D_{1i}L}{u_1 R_1^2}$

Shell side:

$$\overline{D_{3\imath}}\left(\frac{\partial^2 \overline{C_{3\imath}}}{\partial \bar{r}^2} + \frac{1}{r + R_2/\delta_2}\frac{\partial \overline{C_{3\imath}}}{\partial \bar{r}}\right) - \frac{\partial \overline{C_{3\imath}}}{\partial \bar{l}} - \Sigma Rkn^* = 0$$

$where \qquad \overline{D_{1\imath}} = \dfrac{\varepsilon_3 D_{3i}L}{u_3 \delta_2^2}$

Table 5.7. Binary and effective diffusivities estimations

Estimation of binary diffusivities with H_2O:

$$\frac{pD_{AB}}{(p_{cA}p_{cB})^{\frac{1}{3}}(T_{cA}T_{cB})^{\frac{5}{12}}\left(\frac{1}{M_A}+\frac{1}{M_B}\right)^{\frac{1}{2}}} = 3.640\times10^{-4}\left(\frac{T}{\sqrt{T_{cA}T_{cB}}}\right)^{2334}$$

Estimation of binary diffusivities with the rest of the components:

$$D_{AB} = 0.0018583\times\frac{\sqrt{T^3\left(\frac{1}{M_A}+\frac{1}{M_B}\right)}}{p\sigma_{AB}^2\Omega_{\mathrm{D,AB}}}$$

$$\sigma_{AB} = \frac{1}{2}(\sigma_A+\sigma_B)$$

$$\frac{E_{AB}}{K} = \sqrt{\frac{E_A}{K}\frac{E_B}{K}}$$

Estimation of effective diffusivities:

$$\frac{1-x_1}{D_{1m}} = \sum_{\mathrm{j=2}}^{\mathrm{n}}\frac{\mathrm{x_j}}{\mathrm{D_{1j}}}$$

5.3. Results and Discussion

5.3.1. Comparison of experimental and modeling studies on the performances of the MR and the PBR

The effect of pressure on the steam reforming of methane in the conventional packed-bed reactor and the membrane reactor is presented at 873 K and 923 K in Figure 5.2. The methane conversions were predicted by using the one-dimensional and two-dimensional models described in the previous section and also compared with the experimental values at both temperatures. For both the packed-bed reactor and the membrane reactor the experimental methane conversions declined with pressure at 873 K and 923 K. This is in accordance with Le Chatelier's principle as the stoichiometries of reactions (1) and (3) for methane reforming indicate a net increase in moles which is disfavored with increasing pressure. It was also found experimentally that the membrane reactor produced higher conversions than the packed-bed reactor at all pressures. This again followed for Le Chatelier's principle, as selective removal of the product hydrogen through the membrane shifts the equilibrium of the reforming and water-gas shift reactions (1)-(3) to the product side and increase the methane conversion. The methane steam reaction is an endothermic reaction overall and favored by temperature and higher conversions were obtained at 923 K than at 873 K.

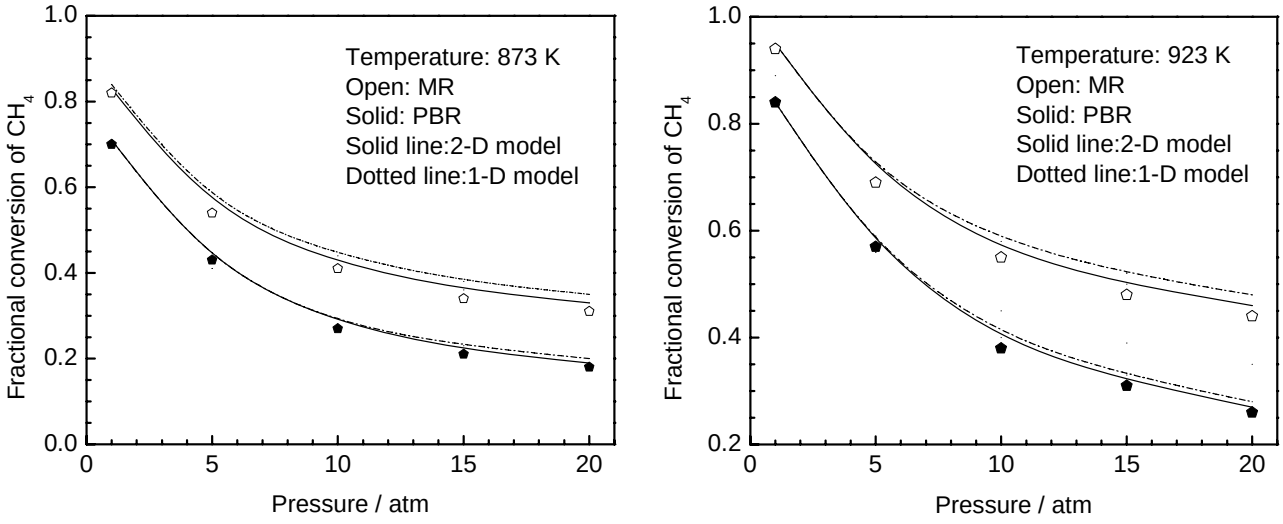

Figure 5.2. a) Fractional conversion of CH_4 in the PBR and the MR at 873 K,

b) Fractional conversion of CH_4 in the PBR and the MR at 923 K

The one-dimensional and the two-dimensional models were able to reproduce all these trends and the experimental values fairly well for both reactor systems. Considering that there were no adjustable parameters in either model, this is a substantial accomplishment. It indicates that both descriptions captured the essential physical phenomena that are occurring in the reactors. As the pressure of the reaction increased, the estimates of conversion for both models were slightly higher than the experimental values. Comparing the two models, the two-dimensional treatment gave a closer agreement to the experimental data for the membrane reactor but both models did equally well with the packed-bed reactor.

The experimental consumption rates of CH_4 and H_2O in the PBR and the MR at 873 K and 923 K are represented in Figure 5.3. The experimental consumption rates in the PBR were much lower than the equilibrium values and leveled off with increasing pressures. The trends in the consumption rate in the PBR and the MR are similar at lower pressures but deviate at higher pressures. The consumption rates both in the PBR and the MR both as pressure was increased from 1 atm, but the rates in the PBR leveled off at higher pressures whereas those in the MR continued rising. At 873 K and atmospheric pressure (Figure 5.3a) consumption rates of CH_4 and H_2O in the MR (CH_4: 5.6×10^{-6} mol s^{-1}, H_2O: 9.5×10^{-6} mol s^{-1}) were slightly higher than the consumption rates observed in the PBR (CH_4: 5.0×10^{-6} mol s^{-1}, H_2O: 8.2×10^{-6} mol s^{-1}). At 20 atm the consumption rates of CH_4 and H_2O in the MR (CH_4: 42.0×10^{-6} mol s^{-1}, H_2O: 83.0×10^{-6} mol s^{-1}) were significantly higher than those in the PBR (CH_4: 25.5×10^{-6} mol s^{-1}, H_2O: 47.3×10^{-6} mol s^{-1}). At 923 K and atmospheric pressure consumption rates of CH_4 and H_2O in the MR (CH_4: 6.3×10^{-6} mol s^{-1}, H_2O: 9.9×10^{-6} mol s^{-1}) were slightly higher than those in the PBR (CH_4: 6.0×10^{-6} mol s^{-1}, H_2O: 9.0×10^{-6} mol s^{-1}). At 20 atm the consumption rates of CH_4 and H_2O in the MR (CH_4: 55.9×10^{-6} mol s^{-1}, H_2O: 98.5×10^{-6} mol s^{-1}) were significantly higher than those in the PBR (CH_4: 35.6×10^{-6} mol s^{-1} g^{-1}, H_2O: 63.2×10^{-6} mol s^{-1}). In general the consumption rate of H_2O was found to be higher than that of CH_4. This is because H_2O is used not only in the reaction with CH_4 (reforming) but also in the reaction with CO (WGS).

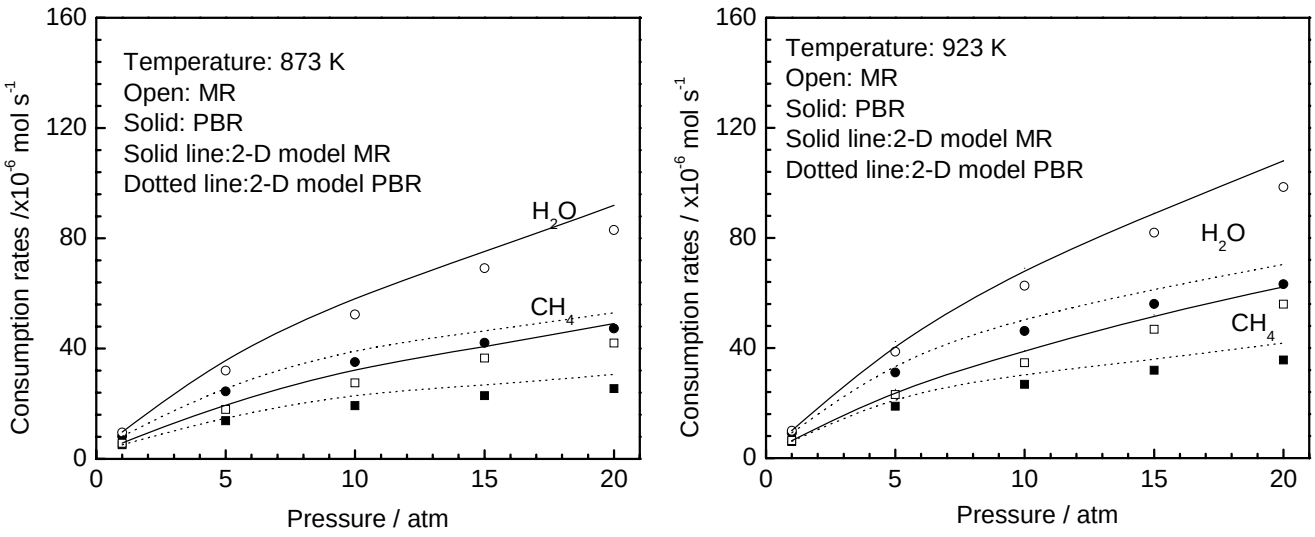

Figure 5.3. a) Consumption rates of CH_4 and H_2O in the PBR and the MR at 873 K, b) Consumption rates of CH_4 and H_2O in the PBR and the MR at 923 K

Figure 5.3 compares the calculated consumption rates obtained from the two-dimensional model with the experimental values. The two-dimensional model was chosen over the one-dimensional one because it performed better in the comparison of the methane conversions as discussed above. At atmospheric conditions, the estimated consumption rates CH_4 and H_2O in the MR (CH_4: 5.7×10^{-6} mol s^{-1}, H_2O: 9.7×10^{-6} mol s^{-1}) closely match the experimental values in the MR (CH_4: 5.6×10^{-6} mol s^{-1}, H_2O: 9.5×10^{-6} mol s^{-1}) at 873 K. At a higher pressure of 20 atm, the estimated consumption rates CH_4 and H_2O in the MR (CH_4: 49.1×10^{-6} mol s^{-1}, H_2O: 92×10^{-6} mol s^{-1}) were a little higher than the experimental values in the MR (CH_4: 42.0×10^{-6} mol s^{-1}, H_2O: 83.0×10^{-6} mol s^{-1}). At a higher temperature of 923 K, the experimental consumption rates of CH_4 and H_2O (CH_4: 6.3×10^{-6} mol s^{-1}, H_2O: 9.9×10^{-6} mol s^{-1}) and the estimated values for CH_4 and H_2O (CH_4: 6.4×10^{-6} mol s^{-1}, H_2O: 10.0×10^{-6} mol s^{-1}) in the membrane reactor are higher than

the respective values in the membrane reactor at 873 K. The estimated consumption rates CH_4 and H_2O in the membrane reactor (CH_4: 62.2×10^{-6} mol s^{-1}, H_2O: 108×10^{-6} mol s^{-1}) are also a little higher than the experimental values in the membrane (CH_4: 55.9×10^{-6} mol s^{-1}, H_2O: 98.5×10^{-6} mol s^{-1}) at 923 K and at 20 atm.

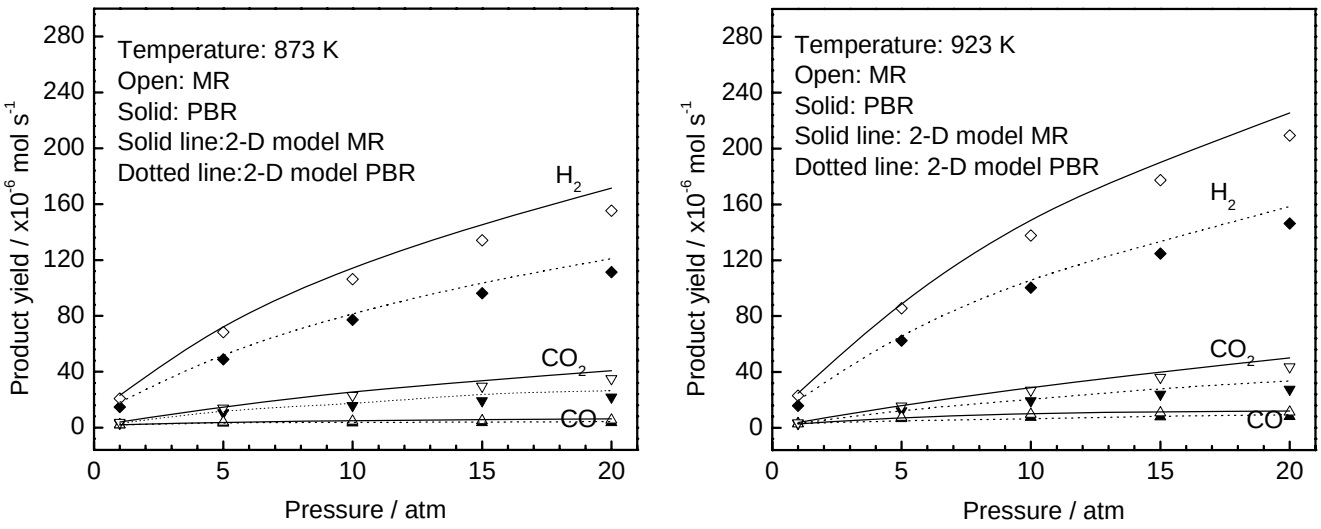

Figure 5.4. a) Yields of H_2, CO and CO_2 in the PBR and the MR at 873 K,
b) Yields of H_2, CO and CO_2 in the PBR and the MR at 923 K

Figure 5.4 shows that the experimental yields of H_2, CO and CO_2 in the MR were above those obtained in the PBR at all pressures at 873 K and 923 K. The CO and CO_2 yields in the membrane reactor are only slightly higher than the values obtained in the packed-bed reactor while the H_2 yields are much higher than those obtained in the packed-bed reactor. Even though the increases in the yields of CO and CO_2 are not extreme, that of H_2 is substantial. At 20 atm the yields of H_2, CO and CO_2 in the membrane reactor (H_2: 209.4×10^{-6} mol s^{-1} g^{-1}, CO: 11.3×10^{-6} mol s^{-1}, CO_2: 43.6×10^{-6} mol

s^{-1}) were also higher than those in the packed-bed reactor (H_2: 146.2×10^{-6} mol s^{-1}, CO: 8.0×10^{-6} mol s^{-1}, CO_2: 27.5×10^{-6} mol s^{-1}) at a higher temperature.

The estimated yields from the two-dimensional modeling studies closely matched both the CO and CO_2 yields in the packed bed reactor and also in the membrane reactor. The estimated H_2 yields were similar to the experimental yields in the packed-bed reactor while the estimated ones in the membrane reactor are a little higher than the experimental values at higher pressures. At 923 K, the yields of H_2, CO and CO_2 in the membrane reactor (H_2: 24.7×10^{-6} mol s^{-1} g^{-1}, CO: 2.6×10^{-6} mol s^{-1}, CO_2: 3.6×10^{-6} mol s^{-1}) are comparable to the experimental values (H_2: 22.9×10^{-6} mol s^{-1} g^{-1}, CO: 2.7×10^{-6} mol s^{-1}, CO_2: 3.5×10^{-6} mol s^{-1}) at atmospheric conditions whereas the yields of H_2, CO and CO_2 obtained at 20 atm (H_2: 225.5×10^{-6} mol s^{-1} g^{-1}, CO: 12.0×10^{-6} mol s^{-1}, CO_2: 50.1×10^{-6} mol s^{-1}) are a little higher than the experimental values (H_2: 209.4×10^{-6} mol s^{-1} g^{-1}, CO: 11.3×10^{-6} mol s^{-1}, CO_2: 43.6×10^{-6} mol s^{-1}) especially in the case of hydrogen.

5.3.2. Isothermal two-dimensional model predictions

Figure-5.5 illustrates the concentration profiles across the membrane reactor as a function of dimensionless radius for different pressures in both the tube and the shell sides. As presented in the previous section, the amount of hydrogen produced increased with increasing pressure. The concentration profiles of H_2 in the shell side didn't vary much along the radius of the reactor below 5 atm. Increasing pressure to 10 atm

contributed to the formation of steep profiles along the radius and the concentration of hydrogen reached a higher value in the area close to the shell wall.

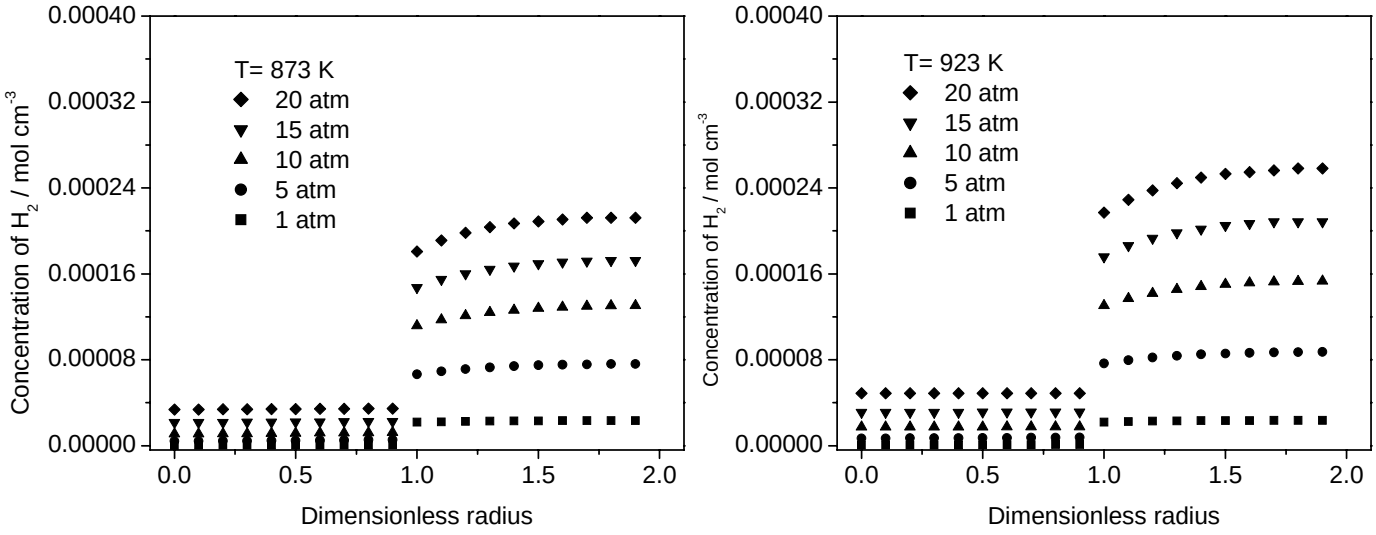

Figure 5.5. a) Radial concentration profiles of hydrogen at 873 K, b) Radial concentration profiles of hydrogen at 923 K

Three dimensional plots of the radial and axial concentration profiles of hydrogen are presented in Figure 5.6. The X-axis represents the radial direction while Y-axis represents the axial direction of the reactor and Z-axis represents the concentration of hydrogen in the membrane reactor. At atmospheric conditions, the concentration of hydrogen flow were almost constant in the radial direction while the concentration of hydrogen both in the shell and tube sides are the lowest at the entrance of the reactor and they increased in both sides through the length of the reactor. At 10 atm, the concentration of hydrogen were much higher when compared to the values obtained at atmospheric pressure. The hydrogen concentrations increased from the entrance of the

reactor to the exit of the reactor in both sides of the reactor. In Figure 5.6c), the concentration profiles of hydrogen obtained at 20 atm are revealed and higher hydrogen production is clearly observable. The decreasing trend closer to the membrane in the shell side and the increasing trend closer to the membrane in the tube side are distinct at this pressure.

The radial and axial concentration profiles obtained at 923 K are shown in Figure 5.7. At atmospheric pressure, constant hydrogen concentration profiles are observed in the shell and the tube side of the reactor which the latter one is much lower that the former one. At a higher pressure of 10 atm, the radial profiles were started to form in the area closer to the membrane. The hydrogen concentration profiles showed an increasing trend especially in the tube side along the reactor. At 20 atm, the hydrogen concentrations were both low at the entrance of the reactor and they started increasing both in the tube and shell sides. The axial hydrogen profile in the tube side was distinct and predicted that the hydrogen separation was the highest at the entrance of the reactor due to the high driving force. On the other hand, the radial profiles demonstrated that the hydrogen flow rates varied especially in the areas closer to the membrane which resulted in steep radial profiles.

The formation of radial profiles in the two-dimensional modeling of the membrane reactor especially pressures higher than 10 atm indicated that the driving force of hydrogen permeation through the membrane was somewhat lower than the one predicted for one-dimensional model. This resulted in lower conversions of methane,

lower consumption rates of methane and hydrogen and reduced hydrogen yields overall and gave an explanation for better prediction performance of the two-dimensional model over the one dimensional one.

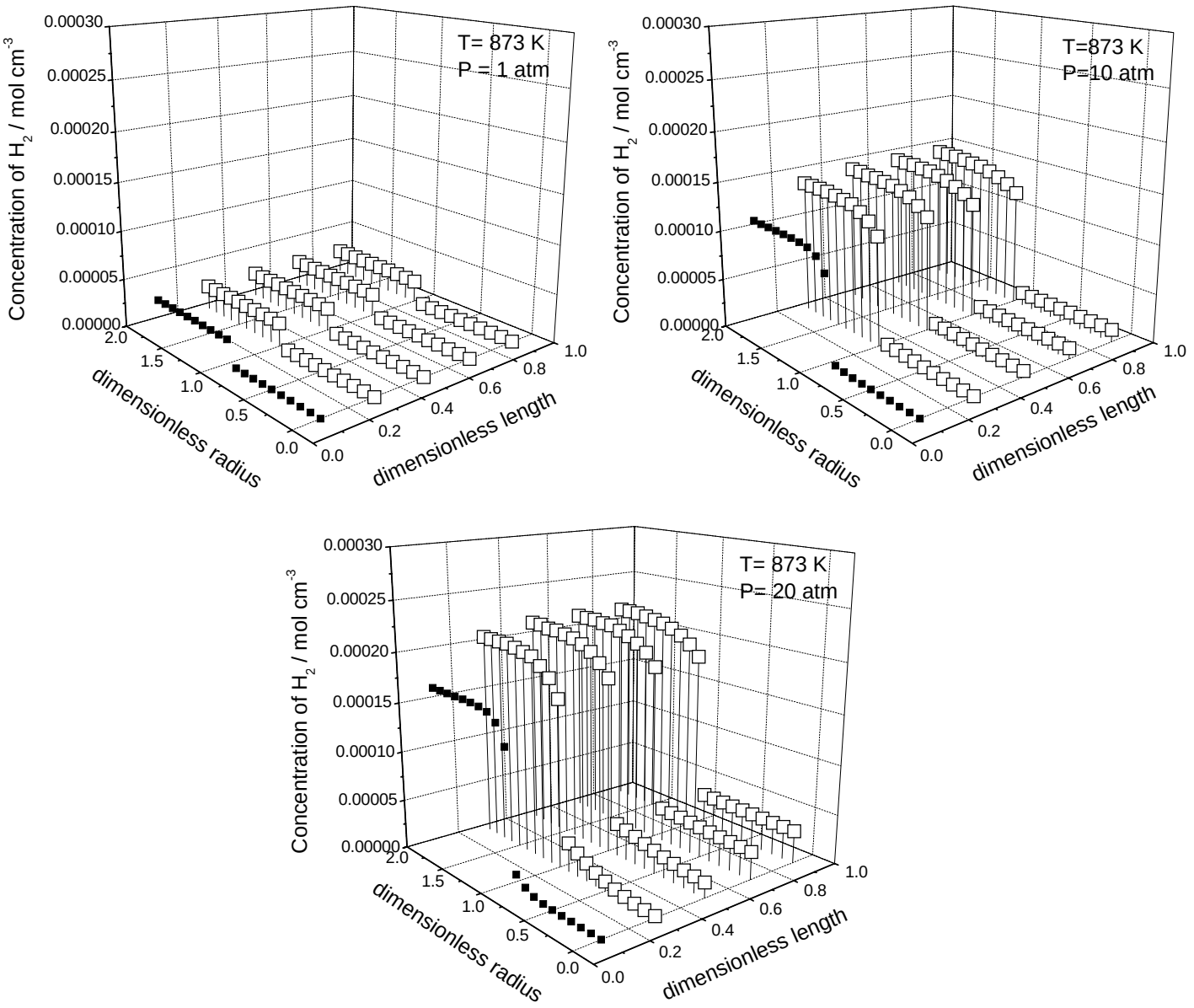

Figure 5.6. a) Radial and axial concentration profiles of hydrogen at 873 K and 1 atm, b) Radial and axial profiles of hydrogen flow at 873 K and 10 atm, c) Radial and axial profiles of hydrogen flow at 873 K and 20 atm

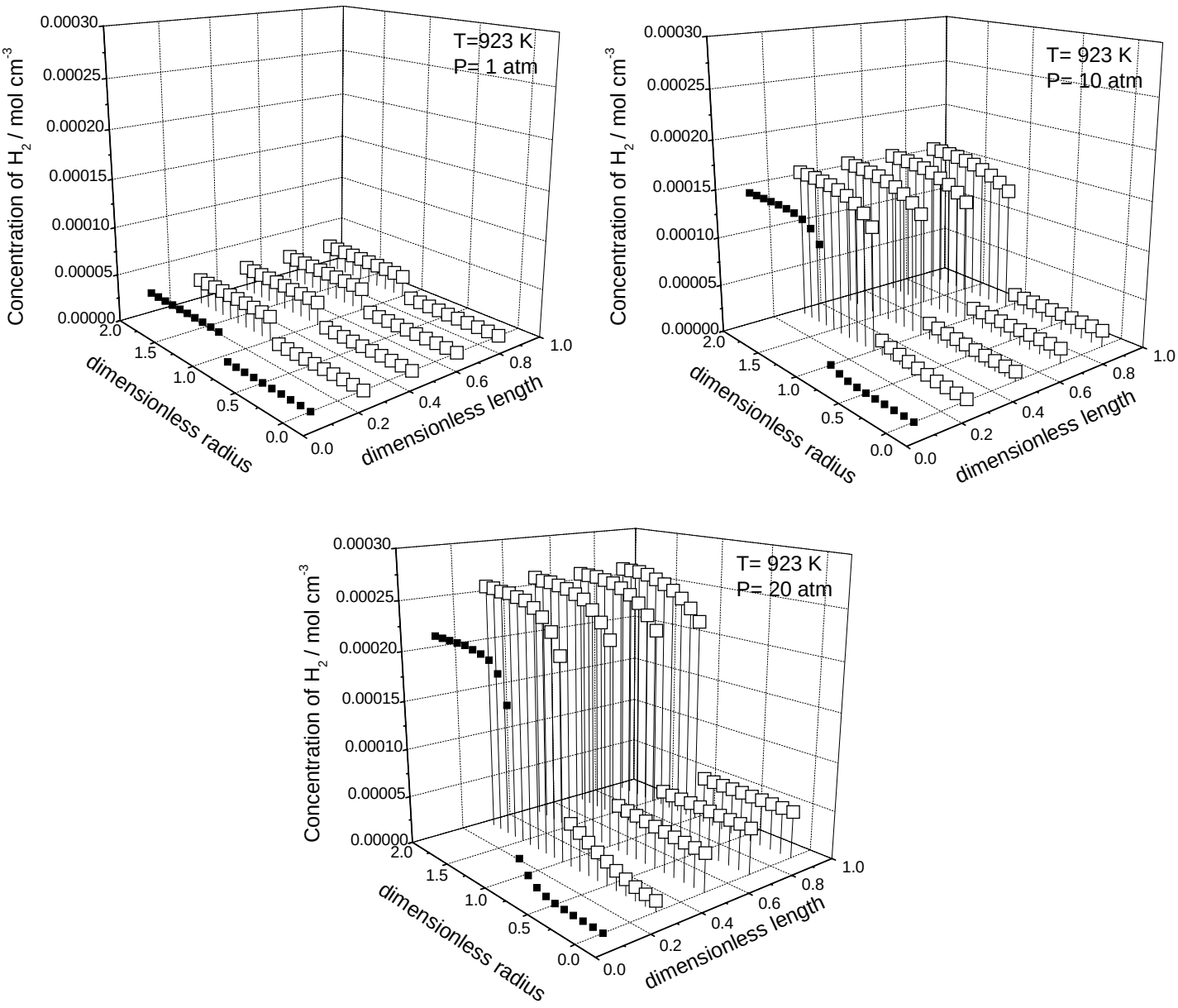

Figure 5.7. a) Radial and axial profiles of hydrogen flow at 923 K and 1 atm, b) Radial and axial profiles of hydrogen flow at 923 K and 10 atm, c) Radial and axial profiles of hydrogen flow at 923 K and 20 atm

5.4. Conclusions

In this study, the methane steam reforming reaction was conducted experimentally in a packed-bed and a membrane reactor at high pressures. A alumina-silica membrane that allows the permeation of hydrogen was used in the membrane reactor. The present work also describes one-dimensional and two-dimensional modeling of the packed-bed and the membrane reactor at the experimental conditions. The one-dimensional and the two-dimensional models were equally capable of predicting the performance of the packed bed reactor. On the other hand, the estimations obtained by using the two-dimensional model were much closer to the experimental values obtained in the membrane reactor. This behavior was clearly observable at high pressures and it arose from a higher driving force for hydrogen permeation. The declining radial profiles through the membrane obtained by the two-dimensional model at high pressures predicted lower hydrogen yields than the one-dimensional model. It is concluded that the radial profiles should be taken into account in the simulation of the membrane reactor at high pressures. These observations are also useful and should be considered in the design of industrial membrane reactors.

References

[1] J. Xu, G. F. Froment, AIChE J. 35 (1989) 88